

Composite active drag control in turbulent channel flows

Jie Yao,^{1,*} Xi Chen,² and Fazle Hussain¹

¹*Texas Tech University, Department of Mechanical
Engineering, Lubbock, Texas, USA, 79409*

²*Key Laboratory of Fluid Mechanics of Ministry of Education,
Beihang University, Beijing, People's Republic of China, 100191*

(Dated: May 5, 2021)

arXiv:2105.01252v1 [physics.flu-dyn] 4 May 2021

Abstract

A composite drag control (CDC) combining the opposition (OC) and spanwise opposed wall-jet forcing (SOJF) methods is studied in a turbulent channel flow via direct numerical simulation of the incompressible Navier–Stokes equations. A maximum drag reduction of about 33% is obtained for CDC – much higher than that produced by either individual method (namely, 19% for SOJF and 23% for OC). Due to the small power input required for both OC and SOJF methods, a significant net power saving (about 32%) is achieved via CDC. Flow analysis shows that CDC can take advantage of both OC and SOJF methods to better suppress drag producing, near-wall turbulent structures – vortices and streaks. In particular, due to the presence of the large-scale coherent swirls generated by SOJF, it is more effective than OC in suppressing the random turbulence. Moreover, due to the OC’s role in suppressing random small-scale turbulence, CDC requires weaker large-scale coherent swirls than those using SOJF only – hence decreasing the drag contribution associated with large-scale swirls. In summary, our results suggest prospects of employing composite control strategy for effective skin friction drag reduction, particularly at very high Reynolds numbers.

I. INTRODUCTION

As the skin friction drag of aircraft and watercraft constitutes a large fraction of the total aerodynamic drag (e.g., approximately 50% of aircraft and about 90% of ships and submarines), its reduction is of great significance for energy saving and environmental protection. Benefited from the continuing improved understanding of flow dynamics [1–3], especially the role of near-wall organized coherent structures, various successful drag control strategies have been proposed. In general, depending on whether external energy is required to drive the control, these strategies fall into two categories [4]: passive and active. For the passive method, riblets are one of the highly investigated approaches and have been shown to yield about 5 – 7% drag reduction in the full-size trials [5]. However, due to the specific requirement, sustenance of the tiny riblets against erosion by atmospheric dust in practical applications is still a challenge. Recently, drag control using superhydrophobic surfaces has been conceived and developed. It has been reported to yield up to 50% and 75% drag reduction in laboratory turbulent channel [6] and boundary layer [7] experiments, respectively.

* Email: jie.yao@ttu.edu

However, as the superhydrophobic surfaces are severely vulnerable to high pressure and high shear rate [8, 9], they have not yet evolved into a practical means.

As for active control methods, they can be further grouped into open- and closed-loop techniques, based on whether sensing is required or not. As one of the simplest open-loop techniques, uniform blowing and suction has been extensively investigated, where uniform blowing is found to reduce the skin friction drag, while uniform suction increases it [10, 11]. The streamwise traveling wave-based (also including spanwise wall oscillations) control strategies are fascinating [12–17], where significant drag reductions are achieved [18–22]. However, considering the typically large amount of power required for actuation, whether effective drag reduction can be obtained at a reasonably high Reynolds number (Re) remains unclear [23, 24]. Streamwise traveling wave-like wall blowing and suction is another typical example of open-loop control techniques. With proper selection of the traveling wave parameters, significant drag reduction and even sub-laminar drag reduction were found in turbulent channel flows [22, 25–27].

One of the promising closed-loop control techniques is the opposition control (OC), which was first studied by Choi *et al.* [18]. Based on the measurements in a plane parallel to the wall (called “detection plane”), OC employs local wall blowing and suction to counteract the sweep and ejection motions induced by the energetic near-wall streamwise vortices. Approximately 25% drag reduction was achieved in turbulent channel flow at friction Reynolds number $Re_\tau (\equiv u_\tau h/\nu) \approx 110$ with the detection plane located at $y_d^+ = 10$ [18]. [u_τ is the friction velocity, ν is the kinematic viscosity, and h is the half channel height; the superscript $+$ indicates that the quantity is scaled by the viscous wall units, namely, $y^+ = yu_\tau/\nu$.] Hammond *et al.* [28] later found that the maximum drag reduction is obtained when $y_d^+ = 15$. For a practical application, sensors and actuators need to be wall-based and flush-mounted to avoid parasitic drag. Lee *et al.* [29] developed the suboptimal control that employs information measurable at the wall, e.g., using streamwise wall shear stress, spanwise wall shear stress, and wall pressure. As machine learning is becoming one of today’s most rapidly growing technique, Han and Huang [30] and Park and Choi [31] recently pursued the feasibility of employing the convolutional neural network (CNN) to predict the wall-normal velocities on the detection plane using either spanwise or streamwise wall shear stress obtained from the direct numerical simulation of channel flow. Applying the trained CNNs to turbulent channel flows at low Re , significant amounts of drag reduction can be

achieved. In addition, [Park and Choi \[31\]](#) also found that 15% drag reduction can still be obtained at $Re_\tau = 578$ by applying the CNN trained at $Re_\tau = 180$.

Currently, most of the above-mentioned drag control strategies are targeted at interrupting the self-sustaining cycle [1, 3], where the low-speed streaks are generated via the lift-up effect of faster advecting streamwise vortices leaving streaks as their trails, while the instability/transient growth of low-speed streaks – if sufficiently strong – regenerates the streamwise vortices. At practical, high Re 's, these near-wall features are physically very small; hence effective control of them becomes rather challenging due to the tiny size of the appropriate sensors and actuators. In addition, as Re increases, the role of outer large-scale structures becomes more important due to their larger contribution to skin friction [32]. Hence, the efficacy of these near-wall targeted methods decreases with increasing Re [15, 20, 23, 33]. [Samie *et al.* \[34\]](#) examined the coherence between a measurable wall quantity (e.g., the wall-shear stress fluctuations) and the streamwise and wall-normal velocity fluctuations in a turbulent boundary layer. They found that the closed-loop drag reduction scheme targeting near-wall cycle of streaks alone will be of limited success in practice as Re grows. Therefore, attempts have also been made to reduce drag by manipulating large-scale coherent structures in the logarithmic and outer regions of turbulent boundary layers. For example, [Schoppa and Hussain \[35\]](#) developed a conceptually simple open-loop large-scale control strategy. By imposing large-scale counter-rotating streamwise swirls with a relatively small excitation amplitude, 20% drag reduction was obtained in a turbulent channel at $Re_\tau \approx 100$. However, there is an ongoing debate over the effectiveness of the large-scale control method with increasing Re . [Canton *et al.*\[36\]](#) found that the drag reduction decreases with increasing Re and becomes nearly zero at $Re_\tau = 550$. However, [Yao *et al.* \[37\]](#) showed that the negative results found by [Canton *et al.* \[36\]](#) arose from their selection of the channel center height as the fixed value for the location of the control swirl centers. In addition, [Yao *et al.* \[37\]](#) validated the large-scale drag control concept for high Re 's using the near-wall spanwise opposed wall-jet forcing (SOJF), and a detailed physical explanation on the drag reduction mechanism is furnished in Ref. Note that SOJF introduce weak spanwise friction and its mean is zero. [38]. Besides these numerical works, there are several experimental studies on large-scale drag controls using either jet [39, 40] or plasma actuation [41, 42].

Caution should be given to controlling large-scale (LSM) and very large-scale (VLSM)

motions, as recent studies show that suppression of these structures does not yield significant drag reduction. For example, [Abbassi *et al.* \[43\]](#) performed an experimental investigation of closed-loop control of manipulating LSMs and VLSMs, and only 3.2% drag reduction was achieved. This is because, when suppressing these large-scale structures, smaller scales may also be concomitantly altered due to nonlinear scale interaction [\[32, 44\]](#). Hence, at high Re , the simultaneous control of small- and large-scale structures may be required to obtain effective drag reduction. Therefore, we propose a composite drag control (CDC) strategy, where two or more different control methods are combined together and applied simultaneously with the hope of producing better performance. Through energy budget analysis, [Chen *et al.* \[45\]](#) showed that both OC and SOJF can yield notable drag reductions, but with different mechanisms. Their combination is potentially additive and may even be synergistic – thus of interest and is examined in the present work. Moreover, there are two additional considerations for performing such a study. First, as OC and SOJF are effective in suppressing small- and large-scale structures, respectively, their combination may yield a significant drag reduction, even at high Re 's. Second, since both of the two methods require small power inputs to drive the control, the net power saving might become promising for CDC.

The rest of the paper is organized as follows. In the following section, the governing equation, numerical scheme, and control method are described. The drag reduction results are presented in section [III](#). Flow statistics and coherent structures are examined in section [IV](#) to elucidate the underlying mechanism on the variation of skin friction under control. Finally, the concluding remarks are provided in section [V](#).

II. COMPUTATIONAL APPROACH

A. Numerical method

Direct numerical simulations are performed in turbulent channel flows using the code “POONPACK” developed by [Lee and Moser \[46\]](#). In this study, x , y , and z denote the streamwise, wall-normal, and spanwise coordinates, respectively; the corresponding velocity components are u , v , and w . The incompressible Navier-Stokes equations are solved using the method of [Kim *et al.* \[47\]](#), in which equations for the wall-normal vorticity and the Laplacian

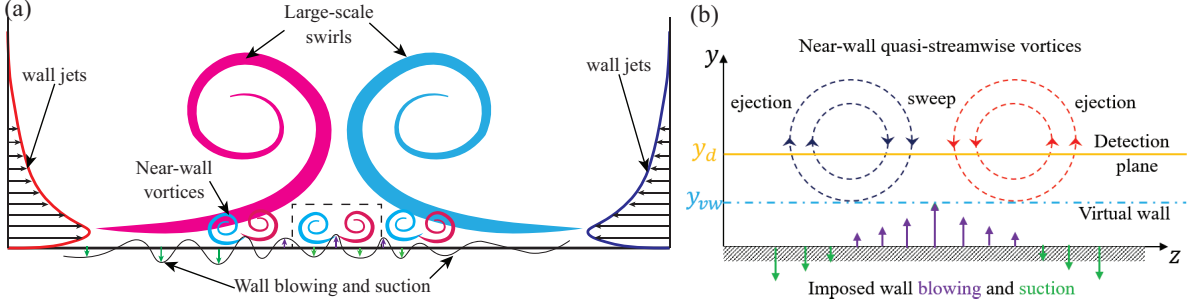


FIG. 1: (a) Schematic of composite drag control (CDC), which combines the spanwise opposite wall jet forcing (SOJF) and the opposition control (OC); (b) the detailed sketch of OC in the near-wall region [dashed box in (a)].

of the wall-normal velocity are time-advanced. This formulation has the advantage of satisfying the continuity constraint exactly while eliminating the pressure. A Fourier-Galerkin method is used in the streamwise and spanwise directions, while the wall-normal direction is represented using a 7th-order B-spline collocation method. A low-storage implicit-explicit scheme based on third-order Runge-Kutta for the nonlinear terms and Crank-Nicolson for the viscous terms are used for time advance. The flow is driven by a pressure gradient, which varies in time to ensure that the mass flux through the channel remains constant. For more details about the code, refer to [Lee and Moser \[46\]](#).

B. Control Schemes

As mentioned in the previous section, CDC consists of OC and SOJF (Fig. 1). For OC, the wall-normal velocity at the wall is set as

$$v_w(x, z, t) = -A_o v(x, y_d, z, t), \quad (1)$$

where A_o is the control amplitude and $v(y_d)$ is the wall-normal velocity at the detection plane y_d (hereinafter, subscript w represents the value on the wall). Such a wall-velocity setting is imposed on both the bottom and the top walls.

Following [Yao *et al.* \[38\]](#), a spanwise forcing is applied for SOJF:

$$F_z = A_s \sin(\beta z) g(y), \quad (2)$$

where A_s is the forcing amplitude, $\beta (= 2\pi/\lambda)$ is the spanwise wavenumber, and $g(y^+)$ is a dimensionless forcing as a function of y . Throughout the paper, all control parameters

TABLE I: Details of the numerical discretization employed for the present simulations. The computational box size is $4\pi h \times 2h \times 2\pi h$ for all cases, and N_x , N_y and N_z are the number of grids in x, y, and z, respectively.

Re_τ	Re_b	$N_x \times N_y \times N_z$	Δx^+	Δy^+	Δz^+
180	2857	$256 \times 192 \times 256$	9.8	0.11	4.7

are normalized in viscous units based on uncontrolled flow (indicated by the subscript 0): a) $A_s^+ = A_s \nu / u_{\tau,0}^3$; b) $\lambda^+ = 2\pi / \beta^+$ ($\beta^+ = \beta \nu / u_{\tau,0}$); and c) $y_c^+ = y_c u_{\tau,0} / \nu$. The forcing function $g(y^+)$ in Eq. (2) is $g(y^+) = y^+ \exp(-\eta y^{+2})$, where the decay factor η in the wall-normal direction specifies the wall-jet velocity profile. The function g has its maximum at $y^+ = y_c^+ = 1/\sqrt{2\eta}$, and y_c^+ represents the height of the spanwise wall-jet maximum velocity. In Eq. (2), g is normalized by its maximum value $g(y_c^+) = y_c^+ \exp(-1/2)$. Note that SOJF is only applied near the bottom wall, but due to its large-scale feature, it is also found to be effective in reducing drag at the top wall.

C. Simulation parameters

DNS is conducted at a fixed bulk Reynolds number $Re_b = U_b h / \nu$, where U_b is the bulk velocity, and the corresponding $Re_\tau \approx 180$. The domain sizes, grid sizes, and resolutions used in the simulations are shown in Table I. The adequacy of the domain size and resolution is confirmed in Refs. [38, 45]. There are, respectively, three and two control parameters for SOJF and OC – a total of five parameters, which make the search for optimal control rather challenging. For simplicity, here we consider only one critical control parameter for each method, namely, A_s for SOJF, and y_d for OC. For other control parameters, we choose the optimal values reported in previous works: namely, $\lambda = 2\pi$ (or, equivalently, $\lambda^+ \approx 1000$) for simultaneous control of about ten streaks and $y_c^+ = 30$ corresponding to the peak of Reynolds shear stress [38], and $A_o = 1$ [18, 28]. In the current study, A_s^+ varies between $[0, 2/3, 4/3, 2, 8/3] \times 10^{-3}$ and $y_d^+ = [0, 5, 10, 15, 20]$. All computations start with the same initial condition of a fully developed turbulent channel flow without control. Time averaging for statistics is taken over at least 25 eddy turnover time (i.e., $tu_\tau/h \geq 25$) after the initial transition.

Due to the presence of large-scale coherent swirls induced by the SOJF, the total flow field can be divided into three components by using the triple decomposition [48]:

$$\mathbf{u}(x, y, z, t) = \mathbf{U}(y) + \underbrace{\tilde{\mathbf{u}}(y, z) + \mathbf{u}''(x, y, z, t)}_{\mathbf{u}'}. \quad (3)$$

Here, \mathbf{u} is the instantaneous total velocity field; $\mathbf{U} = \langle \bar{\mathbf{u}} \rangle$ is the mean velocity, where the overbar indicates averaging in time and in the streamwise direction; and the bracket $\langle \cdot \rangle$ indicates spanwise averaging over one wavelength period; $\mathbf{u}' = \mathbf{u} - \mathbf{U}$ is the total fluctuation; $\tilde{\mathbf{u}} = \bar{\mathbf{u}} - \mathbf{U}$ is the so-called “organized field” representing the coherent motion induced by the swirls of SOJF, and $\mathbf{u}'' = \mathbf{u} - \bar{\mathbf{u}}$ is the random turbulent fluctuation. Note that for OC only, $\tilde{\mathbf{u}}$ is absent, and $\mathbf{u}'' = \mathbf{u}'$.

III. DRAG REDUCTION AND CONTROL EFFICIENCY

We define drag reduction as the relative change in the skin-friction drag coefficient:

$$\mathcal{R} = 1 - C_f/C_{f,0}, \quad (4)$$

where $C_f = 2\tau_w/(\rho_b U_b^2)$ and $C_{f,0} = 2\tau_{w,0}/(\rho_b U_b^2)$ are the drag coefficients of the controlled and reference (uncontrolled) cases, respectively.

Net power saving can be defined as a relative change in the power spent:

$$\mathcal{N} = 1 - (P + W)/P_0, \quad (5)$$

where $P = u_\tau^2 U_b/h$ and $P_0 = u_{\tau,0}^2 U_b/h$ are the pumping power of the controlled and reference (uncontrolled) cases, respectively; and W is the power input due to control, which is given as [45]

$$W = \underbrace{\langle w F_z \rangle}_{W_s} + \underbrace{\langle \rho v_w^3 / 2 \rangle + \langle p_w v_w \rangle}_{W_o}. \quad (6)$$

Here, F_z is the spanwise force given in Eq. 2, and p_w and v_w represent pressure and wall-normal velocity at the wall. W_s and W_o denote the power inputs to the fluid system by SOJF and OC, respectively. For statistical equilibrium or steady state, the total power input is balanced by total dissipation (i.e., $\epsilon = \nu \langle \partial_j u_i \partial_j u_i \rangle$). Hence, the net power saving rate can also be estimated as

$$\mathcal{N} = 1 - \epsilon/\epsilon_0, \quad (7)$$

where ϵ and ϵ_0 denote the dissipation of the controlled and reference (uncontrolled) cases, respectively.

Note that Eq. 6 is the exact mathematical form of the control power input [45]. Defined this way, W can have locally negative values. To ensure that any power input is always associated with energy consumption, several works [49, 50] employ a more conservative form to estimate the power input by taking the absolute values of these quantities before averaging. However, in this work, we use this exact form, as it reflects the true energy flux in the flow systems (see Sec.IV D).

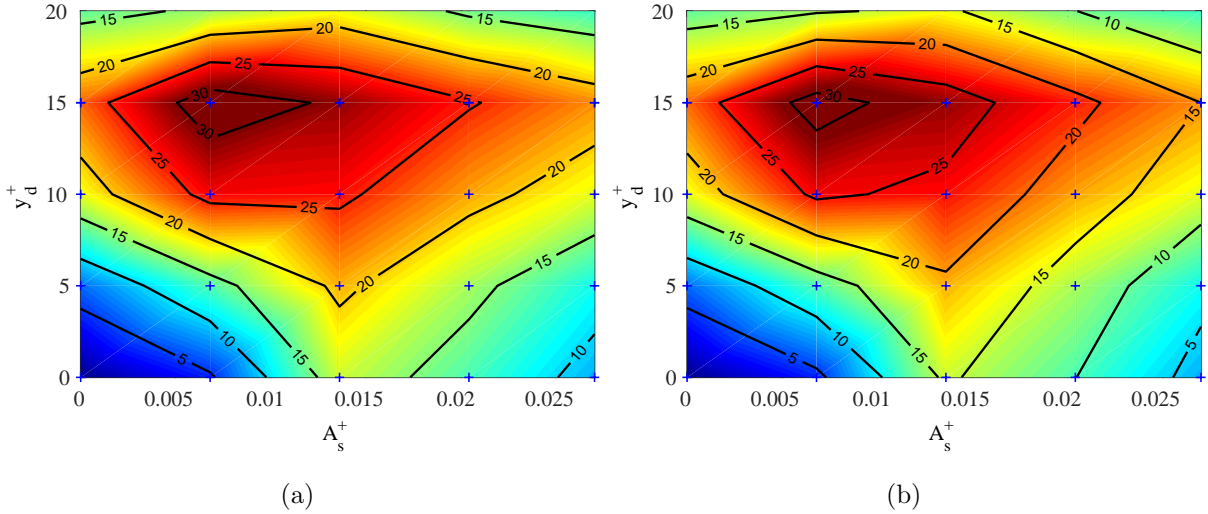


FIG. 2: (a) Drag reduction \mathcal{R} (%) and (b) net power saving \mathcal{N} (%) as functions of A_s^+ and y_d^+ for CDC at $Re_\tau = 180$. The symbol + indicates simulation data points used for interpolation.

Figures 2 (a,b) show the contour plots of drag reduction \mathcal{R} and net power saving \mathcal{N} as functions of A_s^+ and y_d^+ at $Re_\tau = 180$. The contours are computed from a linear interpolation of discrete simulated points (marked as +). Note that cases with $y_d^+ = 0$ ($A_s^+ = 0$) corresponds to the SOJF (OC) only. In addition, figures 3(a,b) show the variation of \mathcal{R} and \mathcal{N} as functions of A_s^+ and y_d^+ , respectively. It is clear from Fig. 2 (a) that significant \mathcal{R} can be achieved in broad ranges of A_s^+ and y_d^+ . For a given A_s^+ , \mathcal{R} first increases then decreases with y_d^+ , and the maximum \mathcal{R} is always obtained at $y_d^+ = 15$ – the optimal value for OC only. For a given y_d^+ , \mathcal{R} also first increases then decreases with A_s^+ . However, different from y_d^+ , the optimal A_s^+ changes and depends on y_d^+ . When $y_d^+ = 0$, the maximum \mathcal{R} is achieved

at $A_s^+ = 0.0013$, which is very close to that reported in Ref. [38]. As y_d^+ increases, the value of A_s^+ that produces maximum \mathcal{R} first decreases and then increases. Within the parameters considered, the maximum \mathcal{R} is 32.5%, with $y_d^+ = 15$ and $A_s^+ = 0.0067$, and the uncertainty, estimated by following the procedure in [23, 38], is approximately 0.5%. Note that as only the variations of y_d^+ and A_s^+ are considered here, a higher \mathcal{R} could possibly be found by varying other control parameters. This is not pursued here due to limited computational resources. It is also worth mentioning that the current studies are performed under the constant flow rate assumption, and, at this low Re , the actually drag reduction amount would be slightly different if the constant pressure gradient assumption is employed [23]. However, the overall behavior of \mathcal{R} as shown in Fig. 2a should remain the same.

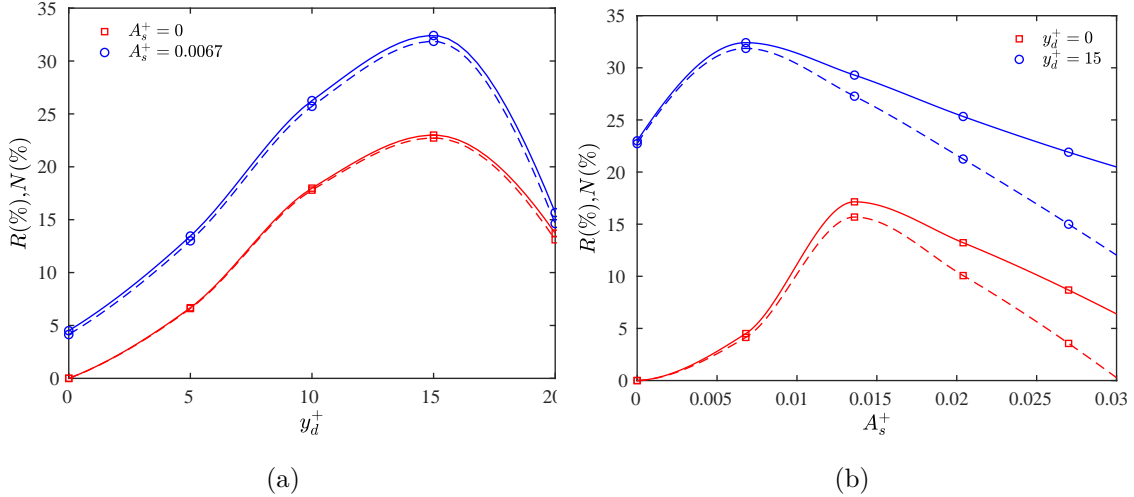


FIG. 3: Drag reduction \mathcal{R} (%) (solid lines) and net power saving \mathcal{N} (%) (dashed lines) as a function of (a) y_d^+ and (b) A_s^+ .

Chen *et al.* [45] showed that compared to other active control techniques, such as spanwise wall oscillation, both OC and SOJF are very promising for net power saving. For OC, the power input W_o increases as y_d^+ increases due to high intensity of wall-normal velocity fluctuations [50]; for SOJF, W_s increases with A_s^+ due to stronger large-scale swirls [38]. However, as both SOJF and OC controls require little power input, notable net power saving can be achieved when combining them together. As shown in Fig. 2, the contour plot of \mathcal{N} is rather similar to those of \mathcal{R} , particularly for small y_d^+ and A_s^+ . Fig. 3 further shows that for a given A_s^+ , \mathcal{N} is only slightly smaller than \mathcal{R} , and for a given y_d^+ , \mathcal{N} slowly deviates from \mathcal{R} with increasing A_s^+ . For the optimally controlled case (i.e., $y_d^+ = 15$ and

$A_s^+ = 0.0067$), approximately 1% of pumping power is needed to actuate the flow control, which results in a maximum \mathcal{N} of 31.5%. Although this high net power saving is impressive, some caution is in order as this value is based only on a simple estimation of the actuation, where the actuator’s energy transfer efficiency (e.g., that of plasma actuators) has not been taken into consideration.

In summary, with the limited parameter search, we demonstrate that the CDC technique could yield a maximum of $\mathcal{R} = 32.5\%$ and $\mathcal{N} = 31.5\%$ – much higher than that can be achieved by either OC or SOJF. This is indeed a very promising finding.

IV. FLOW ANALYSIS

To understand the mechanisms of drag reduction, flow statistics as well as the dynamics are examined in detail below for four cases: Case I, $A_s^+ = 0$ and $y_d^+ = 0$ (uncontrolled); Case II, $A_s^+ = 0$ and $y_d^+ = 15$ (optimal for OC only); Case III, $A_s^+ = 0.0133$ and $y_d^+ = 0$ (optimal for SOJF only); and Case IV, $A_s^+ = 0.0067$ and $y_d^+ = 15$ (optimal for CDC).

A. Near-wall streaks and vortical structures

Figure 4 shows the λ_2 vortices [51] along with the low-speed streaks at $y^+ = 15$. For Case I, the typical meandering low-speed streaky structures are observed aligned along the streamwise direction, and numerous slender vortices are distributed throughout the wall region, lying around the interface between low- and high-speed streaks [figure 4(a)]. For Case II, although the streaks still have typical meandering shapes, their strengths are significantly weakened. Correspondingly, the generation of drag-inducing near-wall streamwise vortices is also suppressed, with fewer vortices as expected. Under SOJF, the basic near-wall streaks are destroyed [Figs. 4(c,d)], and only a single wide meandering streak lies along the mid-span and extends the entire flow length, as expected from the merger of the numerous background streaks forced by the two wall-jets [38]. For Case III, most of the near-wall streamwise vortices disappear, except near the central collision region, just above the merged streak envelope. Consistent with the further suppression of random turbulent fluctuations and associated dissipation, the vortices become fewer for Case IV – clarifying the improved effectiveness of CDC. With OC applied, the near-wall streaks become weak; hence less

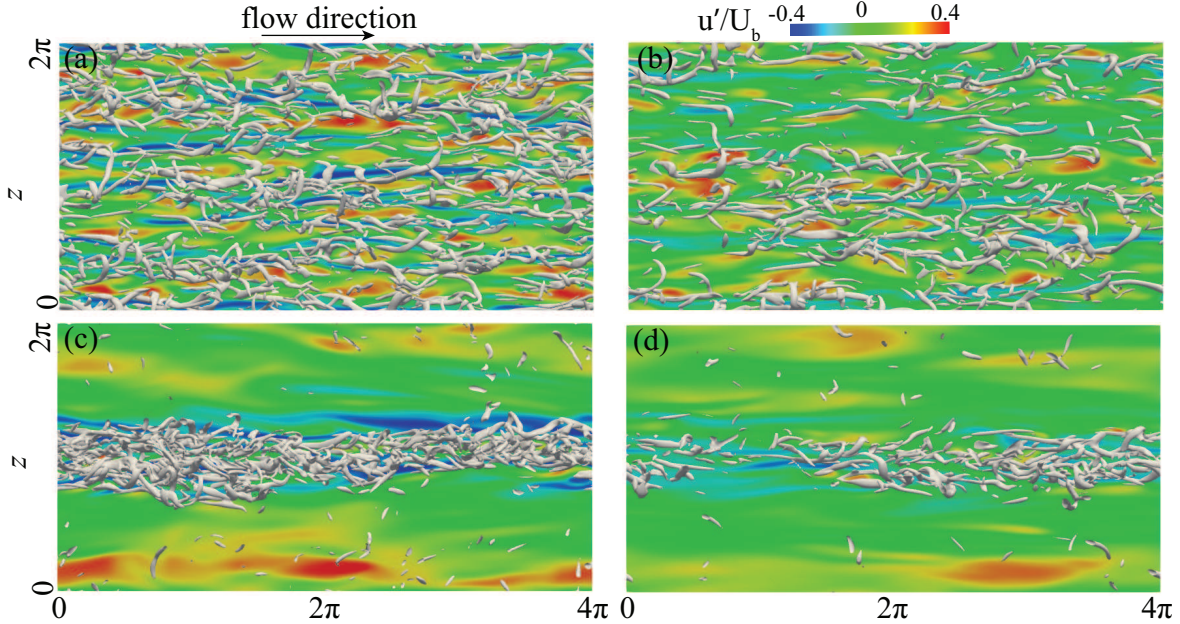


FIG. 4: λ_2 vortical structures associated with the streamwise velocity fluctuations at $y/h = -0.92(y_0^+ = 15)$ on the bottom-half walls for (a) Case I; (b) Case II; (c) Case III; and (d) Case IV.

intensive large-scale swirls are required to merge them together – the reason why the optimal A_s^+ decreases from 0.015 to 0.0067 [Fig. 3(b)].

B. Flow Statistics

Figure 5(a) shows the mean streamwise velocity profile $U^+ (= U/u_\tau)$ in outer units, with Figs. 5(b) and 5(c) showing the same quantity for the bottom and top halves of the channel in the wall units. Compared to the uncontrolled case (i.e., Case I), U^+ profile for Case II (corresponding to the optimal OC case) in the near-wall region is almost unchanged, and U^+ in the log and outer region shows a characteristic upward shift – similar to those observed in Refs. [20, 50]. As the flow in the outer region is barely altered by the OC, the upward shift is mainly attributed to a smaller u_τ ; hence, its magnitude is directly linked to \mathcal{R} . For Case III (corresponding to the optimal SOJF control case), U^+ profile is significantly altered. In particular, due to the presence of large swirls imposed by SOJF near the bottom wall, U^+ is no longer symmetric with respect to the channel centerline, and the peak of U^+ is shifted towards the bottom wall. For Case IV (corresponding to the optimal CDC case), U^+

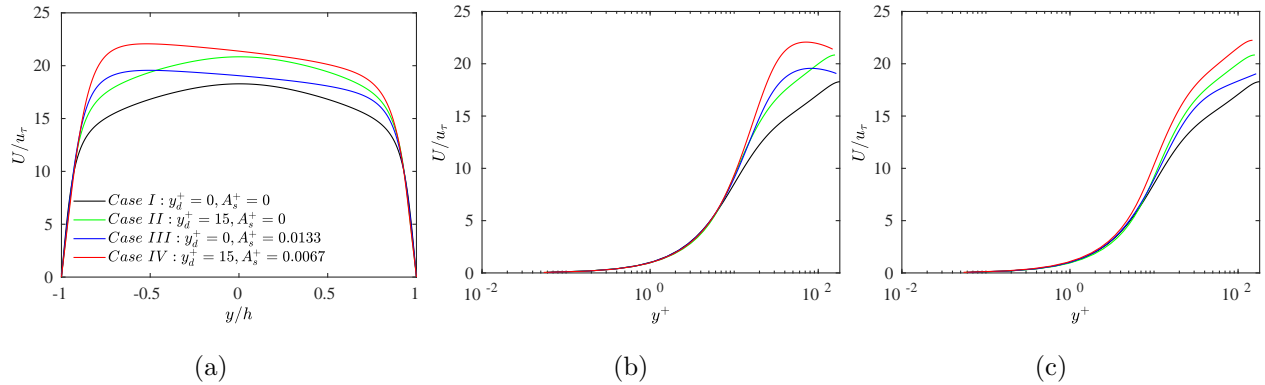


FIG. 5: Mean velocity $U(y)$ for (a) the whole channel, (b) bottom- and (c) top-half channel.

resembles Case III, but with an upward shift.

Figures 6(a) and 6(b) show the cross-streamwise view ($y - z$ plane) of contours of the streamwise velocity and the cross-plane velocity vectors of $\bar{\mathbf{u}}$ for Case III and Case IV, respectively. As discussed in Ref. [38], due to the lift-up effect of the counter-rotating control swirls, a low-speed streak forms for Case III and extends up to the outer flow region ($y/h > -0.5$). Near the wall, however, the streaks have dual peaks – due to the secondary swirls caused by the no-slip wall. As for Case IV, the topmost low-speed streak has a similar shape as Case III. However, due to the presence of OC, the secondary swirls are suppressed; as a result, the dual peaks of the near-wall streaks become less apparent. In addition, due to smaller A_s^+ , the primary counter-rotating swirls are also weaker than that of Case III.

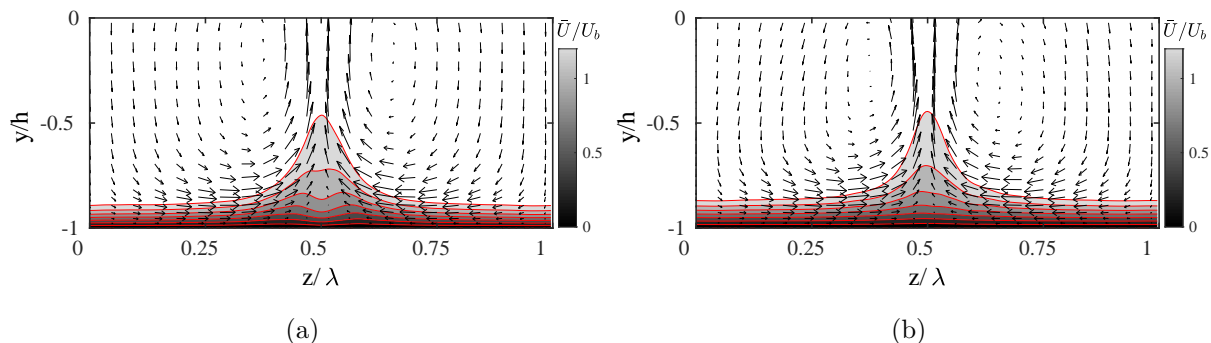


FIG. 6: Cross-stream ($y - z$) plane view of the mean velocity field ($\bar{\mathbf{u}}$) with the contours indicating the mean streamwise velocity (normalized by the bulk velocity U_b), and the vectors denote the wall-normal and spanwise velocities for (a) Case III and (b) Case IV.

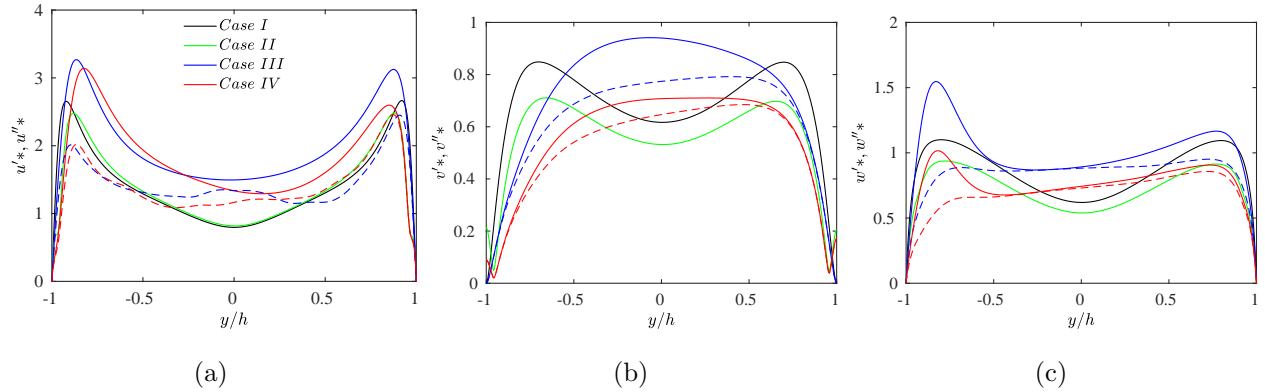


FIG. 7: Root mean square of velocity fluctuations: (a) u'_{rms} ; (b) v'_{rms} ; (c) w'_{rms} . Note that the dashed lines are u''_{rms} and v''_{rms} and w''_{rms} for Cases III and IV.

Figure 7 shows the root mean square (r.m.s) of total velocity fluctuations (u'^* , v'^* , and w'^*) and random velocity fluctuations (u''^* , v''^* , and w''^*). [The superscript $*$ indicates non-dimensionalization by the wall units of the controlled flow]. For Case II, OC establishes a virtual wall as illustrated in Fig. 1b, which is typically located halfway between the physical wall and the sensing plane y_d^+ [18, 20]. The location of the virtual wall y_{vw} can be reflected by a local minimum of v'_{rms} . Turbulent intensities are significantly suppressed near the virtual wall. In particular, v'_{rms} becomes almost zero at $y = y_{vw}$, which inhabits the interaction between the near wall and the outer core regions. As a result, u'_{rms} and w'_{rms} are significantly suppressed below the virtual wall. Compared to the uncontrolled case, the peak location moves away from the wall, consistent with the observation in Refs. [18, 50]. For Case III, although all turbulence intensities (u'_{rms} , v'_{rms} , and w'_{rms}) are suppressed in the near-wall region, they are significantly enhanced in the outer region – mainly due to the increased momentum exchange caused by the presence of large-scale control swirls. For random turbulence velocity fluctuations (u''_{rms} , v''_{rms} , and w''_{rms}), where the effects of large-scale swirls are excluded, the peaks of them become smaller than those of the uncontrolled case. However, they are still slightly larger than the uncontrolled case in the core layer, mainly due to the advection of the large-scale control swirls, which transport the near-wall turbulence and vortical structures to the outer flow. For Case IV, the behaviors of all turbulence intensities are similar to Case III, but with smaller magnitudes – suggesting a better suppression of near-wall streamwise vortices.

C. Skin friction decomposition

The mean skin-friction C_f can be decomposed into different physics-informed contributions based on the mean and statistical turbulence quantities across the wall layer. For example, the FIK (Fukagata, Iwamoto, Kasagi) identity [52, 53] links C_f with the total Reynolds shear stress $\langle \overline{u'v'} \rangle$, which is given as

$$C_f = \underbrace{\frac{6}{Re_b}}_{C_{f,F}^L} + \underbrace{\frac{3}{U_b^2} \int_{-1}^1 y \langle \overline{u'v'} \rangle dy}_{C_{f,F}^T}. \quad (8)$$

The drag coefficient C_f thus has a laminar part $C_{f,F}^L = 6/Re_b$, which is the drag for laminar flow with the same flow rate, and a turbulent part $C_{f,F}^T$, which is represented by the weighted integration of the total Reynolds shear stress (RSS) $\langle \overline{u'v'} \rangle$. As the latter is composed of a coherent $\langle \tilde{u}\tilde{v} \rangle$ and a random part $\langle \overline{u''v''} \rangle$, Eq. 8 can be further decomposed as

$$C_f = \underbrace{\frac{6}{Re_b}}_{C_{f,F}^L} + \underbrace{\frac{3}{U_b^2} \int_{-1}^1 y \langle \tilde{u}\tilde{v} \rangle dy}_{C_{f,F}^C} + \underbrace{\frac{3}{U_b^2} \int_{-1}^1 y \langle \overline{u''v''} \rangle dy}_{C_{f,F}^R}. \quad (9)$$

Since Re_b is held constant for all cases, only changes in the coherent $C_{f,F}^C$ and random $C_{f,F}^R$ contributions affect the drag. Figure 8(a) shows the profiles of the total weighted Reynolds shear stress (WRSS) $-(1-y)\langle \overline{u'v'} \rangle$, and figure 8(b) shows the corresponding coherent part $-(1-y)\langle \tilde{u}\tilde{v} \rangle$ (denoted as C-WRSS) and the random part $-(1-y)\langle \overline{u''v''} \rangle$ (denoted as R-WRSS). Following Eq. (8), for all controlled cases, the drag reduction is mainly due to suppression of Reynolds shear stress in the near-wall region. For Case II, the weighted Reynolds shear stress (WRSS) becomes almost zero at the location of the virtual wall. For Case III, although SOJF is applied only near the bottom wall, the WRSS is also notably decreased near the top wall. Consistent with a larger \mathcal{R} , WRSS for Case IV is significantly suppressed compared to the uncontrolled case, particularly in the bottom half of the channel. Furthermore, from figure 8(b), C-WRSS dominates R-WRSS to become the main contributor to WRSS in the bottom half channel, but the trend reverses in the top half channel. Interestingly, the main difference between Cases III and IV is on C-WRSS. It suggests that when compared to the SOJF, the better performance of CDC is mainly due to smaller Reynolds shear stress associated with the weakened large-scale control swirls.

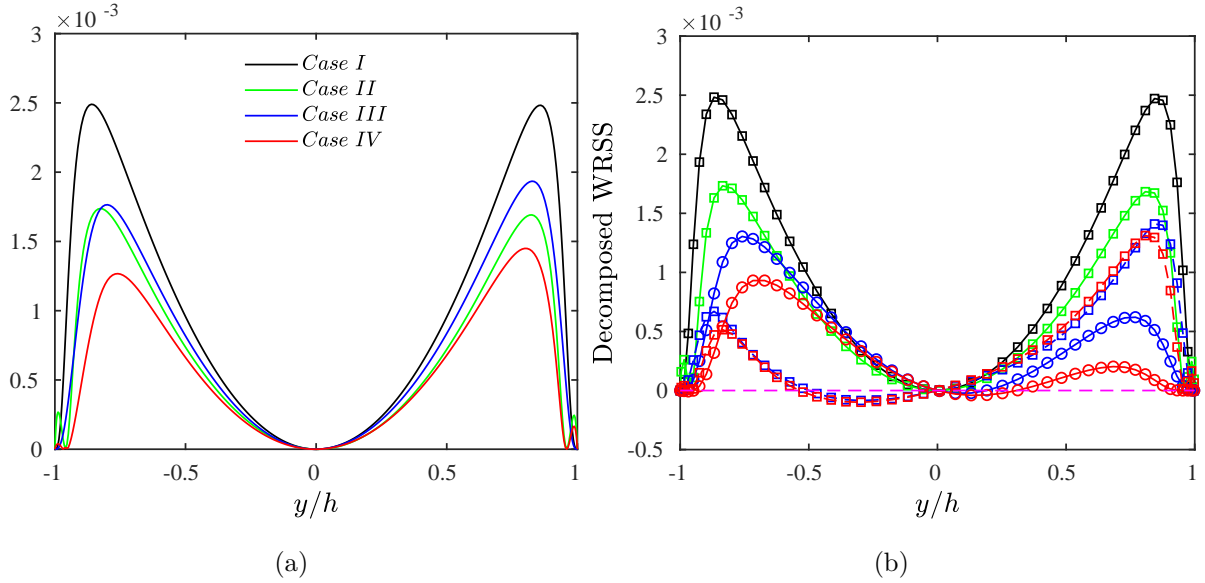


FIG. 8: (a) Total and (b) decomposed weighted Reynolds shear stress (WRSS) distributions for different control cases. The symbols \circ and \square in (b) represent the coherent and random weighted Reynolds shear stress, respectively.

Figure 9(a) shows the decomposed total skin friction (normalized by $C_{f,0}$) based on the FIK identity. For the uncontrolled case (Case I), the laminar ($C_{f,F}^L$) and turbulent ($C_{f,F}^T$) parts contribute 25.8 % and 74.2 % to the total $C_{f,0}$, respectively. For Case II, $C_{f,F}^T$ decreases to approximately 51.1% of $C_{f,0}$. For Case III, the random part $C_{f,F}^R$ contributes only about 24.9% of $C_{f,0}$, while the coherent part $C_{f,F}^C$ becomes the dominant contribution, about 32.1%. When compared to Case III, both $C_{f,F}^R$ and $C_{f,F}^C$ are further decreased for Case IV, contributing about 19.0% and 22.7%, respectively.

The FIK identity are often criticized due to a lack of physical interpretation for the linear weight of Reynolds shear stress. [Renard and Deck \[54\]](#) proposed an alternative mean skin friction decomposition, referred to as the RD identity. It is derived from the mean streamwise kinetic-energy equation in an absolute reference frame and characterizes the power of skin-friction as an energy transfer from the wall to the fluid by means of dissipation by molecular viscosity and turbulent production. In the case of turbulent channel flow, the RD identity can be written as

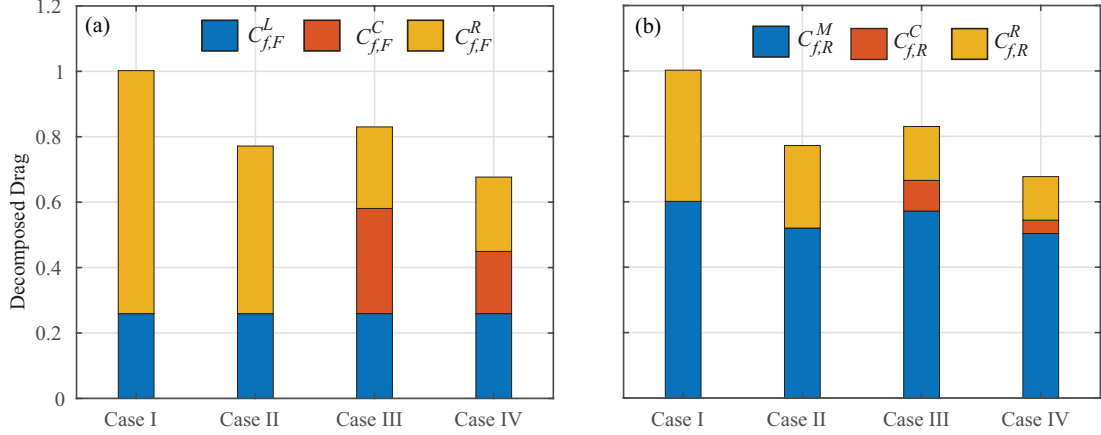


FIG. 9: The skin friction decomposition based on (a) FIK and (b) RD identities for different cases.

$$C_f = \underbrace{\frac{1}{U_b^3} \int_{-1}^1 \nu \left(\frac{\partial U}{\partial y} \right)^2 dy}_{C_{f,R}^M} + \underbrace{\frac{1}{U_b^3} \int_{-1}^1 \langle -u'v' \rangle \frac{\partial U}{\partial y} dy}_{C_{f,R}^T}, \quad (10)$$

$$= \underbrace{\frac{1}{U_b^3} \int_{-1}^1 \nu \left(\frac{\partial U}{\partial y} \right)^2 dy}_{C_{f,R}^M} + \underbrace{\frac{1}{U_b^3} \int_{-1}^1 \langle -\tilde{u}\tilde{v} \rangle \frac{\partial U}{\partial y} dy}_{C_{f,R}^C} + \underbrace{\frac{1}{U_b^3} \int_{-1}^1 \langle -u''v'' \rangle \frac{\partial U}{\partial y} dy}_{C_{f,R}^R}, \quad (11)$$

where $C_{f,R}^M$ represents the contribution from direct molecular viscous dissipation and $C_{f,R}^T$ characterizes the contribution associated with the turbulent-kinematic-energy (TKE) production $\langle -u'v' \rangle (\partial U / \partial y)$. Similarly, the turbulent contribution can be further separated into coherent ($C_{f,R}^C$) and random ($C_{f,R}^R$) parts, which are, respectively, associated with coherent and random Reynolds shear stresses.

Figure 9(b) shows the decomposed total skin friction (normalized by $C_{f,0}$) based on RD identity. For the uncontrolled case (Case I), $C_{f,R}^M$ overwhelm $C_{f,R}^T$ at this low Re , contributing 59.9 % of $C_{f,0}$. Under OC, both $C_{f,R}^M$ and $C_{f,R}^T$ components are decreased to 51.8% and 25.2%, respectively. For case III, although the $C_{f,R}^T$ is almost the same as Case II, the random contribution $C_{f,R}^R$ is only 16.5% – the rest is due to the coherent component $C_{f,R}^C$ that associated with production of the large-scale control swirls. As discussed in Ref. [38], effective drag reduction by SOJF results from a compensative effect of suppressing random turbulence countered by enhancing the coherent part induced by the forcing. For Case IV,

$C_{f,R}^M$ is similar to Case II, but $C_{f,R}^R$ is notably decreased. Compared to Case III, all three contributions are decreased, especially for $C_{C,R}^C$ due to smaller control amplitude. It suggests that, with the aid of OC, SOJF becomes more effective due to the decreased counter effect caused by the large-scale coherent swirls.

D. Energy flux analysis

For a flow system at statistic equilibrium, the rate at which energy enters the system (e.g., pumping power P and control power input W) must equal the rate at which energy is dissipated (i.e., the viscous dissipation ϵ). When employing the Reynolds decomposition, the kinetic energy of the flow can be separated into the kinetic energy of the mean (MKE) and turbulent fields (TKE). In this section, we examine how the energy transfer between the mean flow and the turbulent fluctuations is affected by control.

As suggested by Ricco *et al.* [55], the energy flux can be compactly described using the so-called energy box, sketched in Figure 10a. The pumping power is merely associated with the mean flow, while the energy dissipation is split into parts corresponding to the mean (ϵ_M) and turbulent (ϵ_f) fields. In addition, the energy transfer from the mean to the fluctuating field is embodied by the production of turbulent kinetic energy P_M . P_M acts as a sink for MKE, but as a source for TKE, which is equal to the sum of ϵ_f and W . Hence, in contrast to RD identity, Chen *et al.* [45] provided an alternative expression for C_f in terms of dissipation and control power input, i.e., $C_f = (\epsilon_M + \epsilon_f - W)/U_b^3$. Similar to that shown in Fig. 9b, for the uncontrolled case, 59.9% and 40.1% of the energy that enters the system (through pumping power) are dissipated by the mean and turbulent fields, respectively. With control, the pumping power is decreased and the amount of decrease corresponds to the rate of drag reduction \mathcal{R} presented in Sec. III. Furthermore, the change of total dissipation ($\epsilon_M + \epsilon_f$) is the rate of net power saving \mathcal{N} [45].

For all the control cases, the dissipation due to the mean flow fields ϵ_M does not change much, which contributes slightly above 50% of P_0 . As a reference, the dissipation due to the laminar mean flow is about one-fourth of P_0 [56]. Unlike ϵ_M , the dissipation due to the turbulent field ϵ_f vastly decreases under control – suggesting significant suppression of near-wall random streamwise vortices. It is of particular interest to look at Case IV, where the control power input W ($= 0.8\%$) is in between Case II ($W = 0.3\%$) and Case III ($W = 1.5\%$),

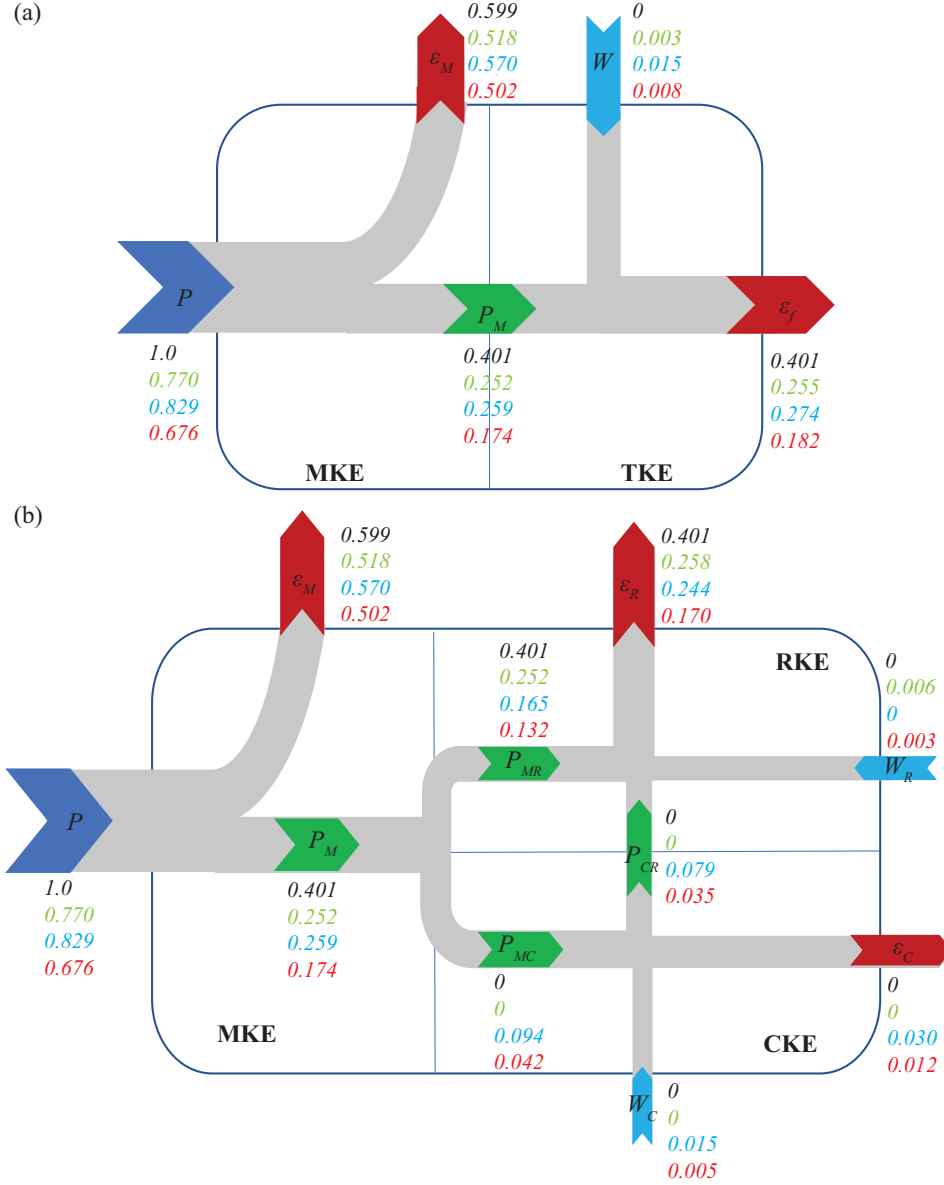


FIG. 10: Energy flux box by (a) Reynolds decomposition and (b) triple decomposition.

Abbreviations MKE, TKE, CKE and RKE represent mean, turbulent, coherent, and random kinetic energies, respectively. All the budget terms have been normalized by the pumping power of the uncontrolled case, and their numerical values for Cases I to IV are presented in order.

but ϵ_f is much smaller than these two cases.

To better understand how control flow affects the energy transfer, [Gatti et al. \[56\]](#) developed an elaborated energy flux analysis by separating the mean flow into a laminar compo-

ment and a deviation from it. Although it provides some further insight on the effect of control on energy flux, it lacks a physical basis to separate the mean flow into laminar mean and the remaining parts. Differently, [Chen *et al.* \[45\]](#) introduced a triple-decomposition (eq. 3) into the energy budget analysis, which enables us to examine how controls affect the energy transfer among the mean, coherent, and turbulent fields. The corresponding energy box is shown in Fig. 10b. For flow under control, the control power can be injected either through random velocity field W_R (e.g., for OC) or through coherent velocity field W_C (e.g., for SOJF). Meanwhile, production converts mean flow energy to both coherent (P_{MC}) and random (P_{MR}) velocity fields. There is an additional production (P_{CR}) associated with the energy transfer from coherent to the random velocity field. Note that similar energy budget analysis has recently been employed by [Alessio *et al.* \[57\]](#) to understand drag reduction mechanisms of lubricated turbulent channel flows.

As the coherent part is absent for Cases I and II, the analysis is equivalent to that based on Reynolds decomposition. For both Cases III and IV, the dissipation due to coherent flow field $\epsilon_C (= \overline{\nu \partial_i \tilde{u}_j \partial_i \tilde{u}_j})$ is rather small. For Case III, although the majority of the turbulent production P_M directly goes to the random turbulent field, around 40% of P_M is injected into the coherent field, most of which, together with the coherent control power input W_C , is eventually transferred to the random fields and is dissipated as $\epsilon_R (= \overline{\nu \partial_i u_j'' \partial_i u_j''})$. For Case IV, due to a smaller forcing amplitude A_s^+ , the large-scale control swirls generated are weaker than Case III. As a consequence, the production and dissipation associated with that are significantly decreased. In addition, although the detecting plane y_d^+ is kept the same, the random control power input W_R is decreased compared to Case II. This is not unexpected as the large-scale swirls weaken the low-speed streaks and suppress the random turbulent fluctuations.

V. DISCUSSION AND CONCLUSION

Composite drag control (CDC) based on the opposition control (OC) and spanwise opposed wall-jet forcing (SOJF) methods is investigated via direct numerical simulation of the incompressible Navier–Stokes equations in a turbulent channel flow. A limited parameter search at $Re_\tau = 180$ shows that a maximum \mathcal{R} of 32% can be obtained with $y_d^+ = 15$ and $A_s^+ = 0.0067$, which is much higher than that can be achieved by each individual

method. Furthermore, due to the small power input required, significant net power saving can be achieved. Flow analysis, including skin friction decomposition and flow visualization, reveals that CDC can take advantage of both OC and SOJF methods. In particular, compared to OC, it is more effective in suppressing the random turbulence due to the presence of large-scale coherent swirls generated by SOJF. In addition, compared to SOJF, it requires weaker large-scale coherent swirls due to the role of OC in suppressing random turbulence – hence decreasing the drag contribution associated with these swirls.

The imposition of SOJF improves the coherence between the measurable wall quantities and the velocity fluctuations in the flow. This also indicates that this control strategy could also yield better performance for more practical wall-quantity-based drag control methods, such as the sub-optimal control and those based on machine learning. For most of the drag control methods, the performance decreases as Re increases, mainly due to the increased contributions of large-scale and very-large-scale structures [58]. As OC and SOJF are designed to suppress small- and large-scale structures, respectively, this CDC strategy might be employed as one possible way to overcome the deterioration of drag reduction performance at high Re . All these questions deserve further investigation.

ACKNOWLEDGMENTS

Computational resources provided by Texas Tech University HPCC, TACC Lonestar are acknowledged. We appreciate Lee and Moser for providing us their DNS code, which is used for this study. X.C. appreciates the funding support by the National Natural Science Foundation of China No. 12072012, 11721202, 91952302.

-
- [1] F. Waleffe, On a self-sustaining process in shear flows, *Physics of Fluids* **9**, 883 (1997).
 - [2] J. Jiménez and A. Pinelli, The autonomous cycle of near-wall turbulence, *Journal of Fluid Mechanics* **389**, 335 (1999).
 - [3] W. Schoppa and F. Hussain, Coherent structure generation in near-wall turbulence, *Journal of fluid Mechanics* **453**, 57 (2002).
 - [4] M. Gad-el Hak, *Flow control: passive, active, and reactive flow management* (Cambridge University Press, 2007).

- [5] D. Bechert, M. Bruse, W. v. Hage, J. T. Van der Hoeven, and G. Hoppe, Experiments on drag-reducing surfaces and their optimization with an adjustable geometry, *Journal of fluid mechanics* **338**, 59 (1997).
- [6] J. P. Rothstein, Slip on superhydrophobic surfaces, *Annual Review of Fluid Mechanics* **42**, 89 (2010).
- [7] H. Park, G. Sun, *et al.*, Superhydrophobic turbulent drag reduction as a function of surface grating parameters, *Journal of Fluid Mechanics* **747**, 722 (2014).
- [8] A. Checco, B. M. Ocko, A. Rahman, C. T. Black, M. Tasinkevych, A. Giacomello, and S. Dietrich, Collapse and reversibility of the superhydrophobic state on nanotextured surfaces, *Physical Review Letters* **112**, 216101 (2014).
- [9] A. Rastegari and R. Akhavan, The common mechanism of turbulent skin-friction drag reduction with superhydrophobic longitudinal microgrooves and riblets, *Journal of Fluid Mechanics* **838**, 68 (2018).
- [10] Y. Sumitani and N. Kasagi, Direct numerical simulation of turbulent transport with uniform wall injection and suction, *AIAA journal* **33**, 1220 (1995).
- [11] Y. Kametani and K. Fukagata, Direct numerical simulation of spatially developing turbulent boundary layers with uniform blowing or suction, *Journal of Fluid Mechanics* **681**, 154 (2011).
- [12] W. Jung, N. Mangiavacchi, and R. Akhavan, Suppression of turbulence in wall-bounded flows by high-frequency spanwise oscillations, *Physics of Fluids A: Fluid Dynamics* **4**, 1605 (1992).
- [13] J.-I. Choi, C.-X. Xu, and H. J. Sung, Drag reduction by spanwise wall oscillation in wall-bounded turbulent flows, *AIAA journal* **40**, 842 (2002).
- [14] M. Quadrio, P. Ricco, and C. Viotti, Streamwise-travelling waves of spanwise wall velocity for turbulent drag reduction, *Journal of Fluid Mechanics* **627**, 161 (2009).
- [15] M. Quadrio, Drag reduction in turbulent boundary layers by in-plane wall motion, *Philosophical Transactions of the Royal Society A* , 1428 (2011).
- [16] L. Agostini, E. Toubert, and M. A. Leschziner, Spanwise oscillatory wall motion in channel flow: drag-reduction mechanisms inferred from dns-predicted phase-wise property variations at $Re=1000$, *Journal of Fluid Mechanics* , 606 (2014).
- [17] A. Yakeno, Y. Hasegawa, and N. Kasagi, Modification of quasi-streamwise vortical structure in a drag-reduced turbulent channel flow with spanwise wall oscillation, *Physics of Fluids* **26**, 085109 (2014).

- [18] H. Choi, P. Moin, and J. Kim, Active turbulence control for drag reduction in wall-bounded flows, *Journal of Fluid Mechanics* **262**, 75 (1994).
- [19] J. Kim and T. R. Bewley, A linear systems approach to flow control, *Annu. Rev. Fluid Mech.* **39**, 383 (2007).
- [20] Y. M. Chung and T. Talha, Effectiveness of active flow control for turbulent skin friction drag reduction, *Physics of Fluids (1994-present)* **23**, 025102 (2011).
- [21] B.-Q. Deng and C.-X. Xu, Influence of active control on stg-based generation of streamwise vortices in near-wall turbulence, *Journal of Fluid Mechanics* **710**, 234 (2012).
- [22] H. Mamori, K. Iwamoto, and A. Murata, Effect of the parameters of traveling waves created by blowing and suction on the relaminarization phenomena in fully developed turbulent channel flow, *Physics of Fluids (1994-present)* **26**, 015101 (2014).
- [23] D. Gatti and M. Quadrio, Reynolds-number dependence of turbulent skin-friction drag reduction induced by spanwise forcing, *Journal of Fluid Mechanics* **802**, 553 (2016).
- [24] J. Yao, X. Chen, and F. Hussain, Reynolds number effect on drag control via spanwise wall oscillation in turbulent channel flows, *Physics of Fluids* **31**, 085108 (2019).
- [25] T. Min, S. M. Kang, J. L. Speyer, and J. Kim, Sustained sub-laminar drag in a fully developed channel flow, *Journal of Fluid Mechanics* **558**, 309 (2006).
- [26] R. Moarref and M. R. Jovanović, Controlling the onset of turbulence by streamwise traveling waves. part 1: Receptivity analysis, arXiv preprint arXiv:1006.4594 (2010).
- [27] A. J. Kaithakkal, Y. Kametani, and Y. Hasegawa, Dissimilarity between turbulent heat and momentum transfer induced by a streamwise travelling wave of wall blowing and suction, *Journal of Fluid Mechanics* **886** (2020).
- [28] E. Hammond, T. Bewley, and P. Moin, Observed mechanisms for turbulence attenuation and enhancement in opposition-controlled wall-bounded flows, *Physics of Fluids* **10**, 2421 (1998).
- [29] C. Lee, J. Kim, and H. Choi, Suboptimal control of turbulent channel flow for drag reduction, *Journal of Fluid Mechanics* **358**, 245 (1998).
- [30] B.-Z. Han and W.-X. Huang, Active control for drag reduction of turbulent channel flow based on convolutional neural networks, *Physics of Fluids* **32**, 095108 (2020).
- [31] J. Park and H. Choi, Machine-learning-based feedback control for drag reduction in a turbulent channel flow, *Journal of Fluid Mechanics* **904** (2020).
- [32] M. de Giovanetti, Y. Hwang, and H. Choi, Skin-friction generation by attached eddies in

- turbulent channel flow, *Journal of Fluid Mechanics* **808**, 511 (2016).
- [33] Y.-S. Wang, W.-X. Huang, and C.-X. Xu, Active control for drag reduction in turbulent channel flow: the opposition control schemes revisited, *Fluid Dynamics Research* **48**, 055501 (2016).
- [34] M. Samie, W. Baars, A. Rouhi, P. Schlatter, R. Örlü, I. Marusic, and N. Hutchins, Near wall coherence in wall-bounded flows and implications for flow control, *International Journal of Heat and Fluid Flow* **86**, 108683 (2020).
- [35] W. Schoppa and F. Hussain, A large-scale control strategy for drag reduction in turbulent boundary layers, *Physics of Fluids* **10**, 1049 (1998).
- [36] J. Canton, R. Örlü, C. Chin, and P. Schlatter, Reynolds number dependence of large-scale friction control in turbulent channel flow, *Physical Review Fluids* **1**, 081501 (2016).
- [37] J. Yao, X. Chen, F. Thomas, and F. Hussain, Large-scale control strategy for drag reduction in turbulent channel flows, *Physical Review Fluids* **2** (2017).
- [38] J. Yao, X. Chen, and F. Hussain, Drag control in wall-bounded turbulent flows via spanwise opposed wall-jet forcing, *Journal of Fluid Mechanics* **852**, 678 (2018).
- [39] G. Iuso, M. Onorato, P. G. Spazzini, and G. M. Di Cicca, Wall turbulence manipulation by large-scale streamwise vortices, *Journal of Fluid Mechanics* **473**, 23 (2002).
- [40] M. Cannata, G. Cafiero, and G. Iuso, Large-scale forcing of a turbulent channel flow through spanwise synthetic jets, *AIAA Journal* **58**, 2042 (2020).
- [41] C. W. Wong, Y. Zhou, Y. Li, and Y. Li, Active drag reduction in a turbulent boundary layer based on plasma-actuator-generated streamwise vortices, in *Proceeding of the 9th International Symposium on Turbulence and Shear Flow Phenomena* (2015).
- [42] T. C. Corke and F. O. Thomas, Active and passive turbulent boundary-layer drag reduction, *AIAA Journal* **56**, 3835 (2018).
- [43] M. Abbassi, W. Baars, N. Hutchins, and I. Marusic, Skin-friction drag reduction in a high-reynolds-number turbulent boundary layer via real-time control of large-scale structures, *International Journal of Heat and Fluid Flow* **67**, 30 (2017).
- [44] J. Hwang, J. Lee, H. J. Sung, and T. A. Zaki, Inner–outer interactions of large-scale structures in turbulent channel flow, *Journal of Fluid Mechanics* **790**, 128 (2016).
- [45] X. Chen, J. Yao, and F. Hussain, Theoretical framework for energy flux analysis of channels under drag control, *Phys. Rev. Fluids* **6**, 013902 (2021).

- [46] M. Lee and R. D. Moser, Direct numerical simulation of turbulent channel flow up to re 5200, *Journal of Fluid Mechanics* **774**, 395 (2015).
- [47] J. Kim, P. Moin, and R. Moser, Turbulence statistics in fully developed channel flow at low reynolds number, *Journal of fluid mechanics* **177**, 133 (1987).
- [48] W. Reynolds and A. Hussain, The mechanics of an organized wave in turbulent shear flow. part 3. theoretical models and comparisons with experiments, *Journal of Fluid Mechanics* **54**, 263 (1972).
- [49] A. Stroh, B. Frohnafel, P. Schlatter, and Y. Hasegawa, A comparison of opposition control in turbulent boundary layer and turbulent channel flow, *Physics of fluids* **27**, 075101 (2015).
- [50] B.-Q. Deng, C.-X. Xu, W.-X. Huang, and G.-X. Cui, Strengthened opposition control for skin-friction reduction in wall-bounded turbulent flows, *Journal of Turbulence* **15**, 122 (2014).
- [51] J. Jeong and F. Hussain, On the identification of a vortex, *Journal of fluid mechanics* **285**, 69 (1995).
- [52] K. Fukagata, K. Iwamoto, and N. Kasagi, Contribution of reynolds stress distribution to the skin friction in wall-bounded flows, *Physics of Fluids (1994-present)* **14**, L73 (2002).
- [53] A. Rastegari and R. Akhavan, On the mechanism of turbulent drag reduction with superhydrophobic surfaces, *Journal of Fluid Mechanics* **773** (2015).
- [54] N. Renard and S. Deck, A theoretical decomposition of mean skin friction generation into physical phenomena across the boundary layer, *Journal of Fluid Mechanics* **790**, 339 (2016).
- [55] P. Ricco, C. Ottonelli, Y. Hasegawa, and M. Quadrio, Changes in turbulent dissipation in a channel flow with oscillating walls, *Journal of Fluid Mechanics* **700**, 77 (2012).
- [56] D. Gatti, A. Cimarelli, Y. Hasegawa, B. Frohnafel, and M. Quadrio, Global energy fluxes in turbulent channels with flow control, *Journal of Fluid Mechanics* **857**, 345 (2018).
- [57] R. Alessio, Z. Francesco, and S. Alfredo, Energy balance in lubricated drag-reduced turbulent channel flow, *Journal of Fluid Mechanics* **Accepted** (2021).
- [58] I. Marusic, R. Mathis, and N. Hutchins, Predictive model for wall-bounded turbulent flow, *Science* **329**, 193 (2010).